

Quantum oscillations in $TaCo_2Te_2$ thin flakes

Ruiyang Jiang(蒋睿阳), Tian Le(乐天), Yunteng Shi(石云腾), Changcun Li(李长存), Xinyi Zheng(郑新义), Xingchen Guo(郭兴宸), Bingbing Tong(仝冰冰), Peiling Li(李沛岭), Ziwei Dou(窦子威), Xiaohui Song(宋小会), Jie Shen(沈洁), Zhaozheng Lyu(吕昭征), Guangtong Liu(刘广同), Fucai Liu(刘富才), Li Lu(吕力), and Fanming Qu(屈凡明)
Citation: Chin. Phys. B, 2025, 34 (**8**): 087307. DOI: 10.1088/1674-1056/add5ce
http://cpb.iphy.ac.cn; http://iopscience.iop.org/cpb

What follows is a list of articles you may be interested in

In-plane negative magnetoresistance and quantum oscillations in van der Waals antiferromagnet $DyTe_3$

Qi Qi(齐琦), Senhao Lv(吕森浩), Ke Zhu(祝轲), Yaofeng Xie(谢耀锋), Guojing Hu(胡国静), Zhen Zhao(赵振), Guoyu Xian(冼国裕), Yechao Han(韩烨超), Yang Yang(杨洋), Lihong Bao(鲍丽宏), Xiao Lin(林晓), Hui Guo(郭辉), Haitao Yang(杨海涛), and Hong-Jun Gao(高鸿钧)
Chin. Phys. B, 2025, 34 (**7**): 077305. DOI: 10.1088/1674-1056/adcc87

Magnetic and magnetotransport properties of layered $TaCoTe_2$ single crystals

Ming Mei(梅明), Zheng Chen(陈正), Yong Nie(聂勇), Yuanyuan Wang(王园园), Xiangde Zhu(朱相德), Wei Ning(宁伟), and Mingliang Tian(田明亮)
Chin. Phys. B, 2023, 32 (**12**): 127303. DOI: 10.1088/1674-1056/acd10a

Nonlinear current response and electric quantum oscillations in the Dirac semimetal Cd_3As_2

Hao-Nan Cui(崔浩楠), Ze-Nan Wu(吴泽南), Jian-Kun Wang(王建坤), Guang-Yu Zhu(祝光宇), Jia-Jie Yang(杨佳洁), Wen-Zhuang Zheng(郑文壮), Zhi-Min Liao(廖志敏), Shuo Wang(王硕), Ben-Chuan Lin(林本川), and Dapeng Yu(俞大鹏)
Chin. Phys. B, 2023, 32 (**8**): 087306. DOI: 10.1088/1674-1056/acd9c5

Quantum oscillations and nontrivial transport in $(Bi_{0.92}In_{0.08})_2Se_3$

Minhao Zhang(张敏昊), Yan Li(李焱), Fengqi Song(宋凤麒), Xuefeng Wang(王学锋), Rong Zhang(张荣)
Chin. Phys. B, 2017, 26 (**12**): 127305. DOI: 10.1088/1674-1056/26/12/127305

Generation of Fabry-Pérot oscillations and Dirac state in two-dimensional topological insulators by gate voltage

Bin Xu(徐斌), Rao Li(李饶), Hua-Hua Fu(傅华华)
Chin. Phys. B, 2017, 26 (**5**): 057303. DOI: 10.1088/1674-1056/26/5/057303

Quantum oscillations in $TaCo_2Te_2$ thin flakes

Ruiyang Jiang(蒋睿阳)[1,2], Tian Le(乐天)[3,†], Yunteng Shi(石云腾)[1,2], Changcun Li(李长存)[4], Xinyi Zheng(郑新义)[1,2], Xingchen Guo(郭兴宸)[1,2], Bingbing Tong(仝冰冰)[1,5], Peiling Li(李沛岭)[1,5], Ziwei Dou(窦子威)[1], Xiaohui Song(宋小会)[1,5], Jie Shen(沈洁)[1], Zhaozheng Lyu(吕昭征)[1,5], Guangtong Liu(刘广同)[1,5], Fucai Liu(刘富才)[4,6,‡], Li Lu(吕力)[1,2,5,§], and Fanming Qu(屈凡明)[1,2,5,¶]

[1] *Beijing National Laboratory for Condensed Matter Physics, Institute of Physics, Chinese Academy of Sciences, Beijing* 100190, *China*
[2] *School of Physical Sciences, University of Chinese Academy of Sciences, Beijing* 100049, *China*
[3] *Center for Quantum Matter, Institute for Advanced Study in Physics, Zhejiang University, Hangzhou* 310027, *China*
[4] *School of Optoelectronic Science and Engineering, University of Electronic Science and Technology of China, Chengdu* 611731, *China*
[5] *Hefei National Laboratory, Hefei* 230088, *China*
[6] *Yangtze Delta Region Institute (Huzhou), University of Electronic Science and Technology of China, Huzhou* 313098, *China*

(Received 26 March 2025; revised manuscript received 29 April 2025; accepted manuscript online 8 May 2025)

The ternary transition-metal telluride $TaCo_2Te_2$ has been reported to host a topological band structure characterized by a nontrivial Berry phase. While transport properties have been investigated in both bulk crystals and thick flakes (>150 nm), studies on thin flakes (< 100 nm) of this van der Waals (vdW) material remain scarce. We investigate the low-temperature transport properties of $TaCo_2Te_2$ thin flakes by fabricating Hall bar devices on mechanically exfoliated flakes with different thicknesses (15 nm and 90 nm). Temperature-dependent resistance measurements reveal that the 15-nm-thick sample exhibits a lower residual resistivity ratio and Debye temperature compared to the 90-nm-thick one. Magnetotransport measurements under perpendicular magnetic fields up to $\pm$14 T demonstrate lower magnetoresistance, carrier concentration, and mobility in the thinner sample, suggesting increased phonon scattering due to defect-induced disorder. Remarkably, pronounced Shubnikov–de Haas (SdH) oscillations are observed above 8 T in both samples in spite of the defect-induced disorder. Analysis of the Landau fan diagram yields a non-zero Berry phase in both samples, indicating the existence of a topologically non-trivial phase in $TaCo_2Te_2$ thin flakes. Our findings establish $TaCo_2Te_2$ as a promising candidate for exploring intrinsic topological states in layered materials.

Keywords: quantum oscillations, $TaCo_2Te_2$, thin flakes
PACS: 73.61.–r, 73.43.Qt, 75.47.–m, 05.60.Gg
DOI: 10.1088/1674-1056/add5ce **CSTR:** 32038.14.CPB.add5ce

1. Introduction

The ternary transition-metal tellurides (TTMTs) have recently emerged as a promising class of materials demonstrating diverse exotic physical phenomena,[1–7] such as correlated edge states and topologically protected surface states. These intriguing properties establish TTMTs as a versatile quantum material platform for exploring the complex interplay between reduced dimensionality, topological quantum states, and unconventional superconductivity. As a member of the TTMTs, the van der Waals (vdW) $TaCo_2Te_2$ with an orthorhombic structure (space group *Pmcn*) was first synthesized in 1991[8] and predicted to exhibit a Peierls distortion,[9] while maintaining air stability, high mobility, and large magnetoresistance.[10,11] In Ref. [10], the authors also reported visible Peierls distortion along the Co chains, accompanied by enlarged vdW gaps and a potentially tilted antiferromagnetic order. In addition, it has been reported that the magnetoresistance follows the extended Kohler's scaling.[12] Angle-resolved photoemission spectroscopy (ARPES) experiments demonstrated the existence of symmetry-protected eightfold fermions (evidenced by double Dirac cones) and fourfold degenerate van Hove singularities, both arising from the synergy of crystalline and time-reversal symmetries.[13] A recent investigation focusing on bulk single-crystal $TaCo_2Te_2$ has systematically investigated its magnetotransport properties to unveil nontrivial Berry phases originating from its double Dirac cones' topological structure.[14] Through detailed analysis of the Landau level index and phase factor extraction from the Shubnikov–de Haas (SdH) and de Haas–van Alphen (dHvA) quantum oscillations under low-temperature and high-magnetic-field conditions, the study conclusively identified robust non-zero Berry phases across multiple Fermi surface pockets. So far, $TaCo_2Te_2$ has been investigated in both bulk single-crystal and thick flakes (> 150 nm). However, transport studies on vdW $TaCo_2Te_2$ thin flakes (< 100 nm) remain

†Corresponding author. E-mail: tianlephy@zju.edu.cn
‡Corresponding author. E-mail: fucailiu@uestc.edu.cn
§Corresponding author. E-mail: lilu@iphy.ac.cn
¶Corresponding author. E-mail: fanmingqu@iphy.ac.cn

© 2025 Chinese Physical Society and IOP Publishing Ltd. All rights, including for text and data mining, AI training, and similar technologies, are reserved.

scarce, especially regarding quantum oscillations in ultra-thin samples.

In this work, we explore the quantum transport properties of both 15-nm-thick and 90-nm-thick exfoliated $TaCo_2Te_2$ flakes through low-temperature magnetotransport measurements. The 15-nm-thick flake demonstrates a lower residual resistivity ratio (RRR), lower Debye temperature, reduced magnetoresistance, lower carrier concentrations, and lower mobilities, which are attributed to enhanced defect-induced disorder. Strikingly, it exhibits pronounced SdH oscillations despite the presence of defects. Analysis of the Landau fan diagram reveals a non-zero Berry phase in both flakes (-0.752π in the 15-nm one and -0.272π in the 90-nm one), indicating that this material could also host a topologically non-trivial band structure in thin flakes, demonstrating robustness of the topological states against disorder-induced scattering.

2. Experiment

The mechanical exfoliation of $TaCo_2Te_2$ thin flakes was performed through an optimized Blue adhesive plastic film/PDMS stamp protocol. Initially, bulk crystals were subjected to repeated mechanical exfoliation on Blue adhesive plastic film until the flakes reached the target thickness range. Subsequently, a pre-patterned PDMS stamp was employed to selectively transfer the exfoliated flakes. The final transfer step involved precisely aligning the PDMS-stamp-supported samples onto Si/SiO_2 (300 nm) substrates.

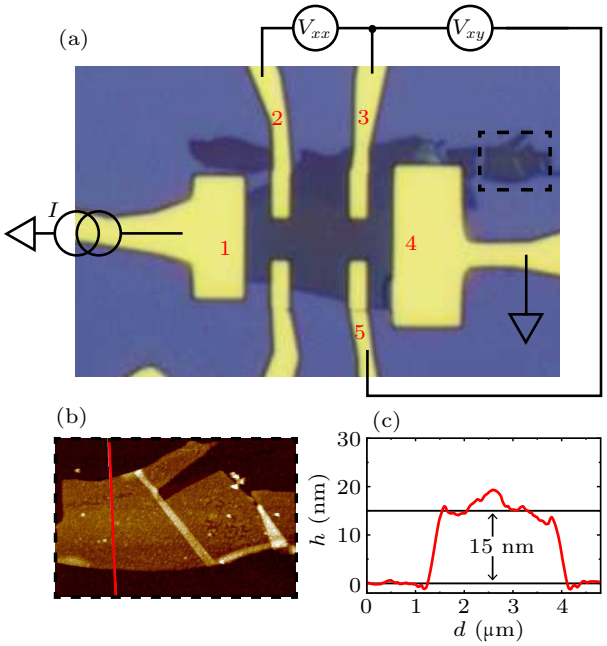


Fig. 1. The Hall bar device #1 fabricated on a 15-nm-thick $TaCo_2Te_2$ flake. (a) Optical image of the Hall bar device #1 and the measurement setup. (b) AFM image corresponding to the black dashed box region in panel (a). (c) Line-cut as marked by the red line in panel (b).

We fabricated Hall bar devices on two $TaCo_2Te_2$ flakes (15 nm and 90 nm thick, respectively) with normal metal electrodes Ti/Au (5 nm/100 nm). As shown in Fig. 1(a), we conducted electrical transport measurements on Hall bar device #1 using electrodes Nos. 1–5 (indicated by the numbers). Lock-in amplifiers (LI5640, NF Corporation) were employed to introduce a small AC current excitation I_{ac} and to measure the longitudinal voltage V_{xx} and Hall voltage V_{xy}. Figures 1(b) and 1(c) present the atomic force microscopy (AFM) measurement of the sample thickness (device #1) of approximately 15 nm.

3. Results and discussion

Figure 2(a) shows the metallic behavior of the normalized resistance $R/R_{1.5\ \mathrm{K}}$ as a function of temperature (T) under zero magnetic field, exhibiting an $RRR = R(300\ \mathrm{K})/R(1.5\ \mathrm{K})$ of ~ 9. We employed the well-established Bloch–Grüneisen formula to fit the R–T curve, an approach previously documented in electrical transport studies of $TaCo_2Te_2$ singlecrystals:[12,14]

$$\rho(T) = \rho_0(0) + A\left(\frac{T}{\theta_D}\right)^n \int_0^{\theta_D/T} \frac{x^n}{(e^x-1)(1-e^{-x})}\,dx, \quad (1)$$

where ρ_0, A, and θ_D are the residual resistivity, electron–phonon interaction constant, and Debye temperature, respectively. Since $R(T)/R(1.5\ \mathrm{K}) = \rho(T)/\rho(1.5\ \mathrm{K})$, during fitting, both sides of Eq. (1) need to be divided by $\rho(1.5\ \mathrm{K}) = 8.20\ \mu\Omega\cdot\mathrm{cm}$. The integer constant n takes values of 2, 3, or 5, corresponding to electron–electron, electron–magnon, and electron–phonon scattering mechanisms, respectively. This formula with $n = 5$ fits the experimental data well from 1.5 K to 80 K, as shown by the red solid line in Fig. 2(a), indicating the dominance of electron–phonon scattering in this temperature range. The fitting yields $\rho_0 = 7.95 \pm 0.02\ \mu\Omega\cdot\mathrm{cm}$, $A = 199.1 \pm 0.2\ \mu\Omega\cdot\mathrm{cm}$, and $\theta_D = 155 \pm 0.1$ K. Notably, the Debye temperature extracted from the R–T curve of device #1 shows a significant reduction compared to previously reported values.[12,14] We will discuss this discrepancy in detail later. At higher temperatures, $\rho(T)$ is lower than that expected from Eq. (1), which was reported to be caused by a thermally induced increase in the charge carrier densities.[12]

We measured the transverse Hall resistivity ρ_{xy} and the longitudinal resistivity ρ_{xx} with the magnetic field applied perpendicular to the film plane ($B\perp$film) from -14 T to 14 T. The longitudinal magnetoresistance $[MR = (\rho_{xx}(B) - \rho_{xx}(0))/\rho_{xx}(0)]$ as a function of B is shown in Fig. 2(b). At 9 T and 1.5 K, the MR attains 72% and its scaling behavior demonstrates excellent agreement with a power-law dependence $MR \propto B^{1.5}$, consistent with the post-annealed sample ($MR \propto B^{1.49}$) in Ref. [11]. Next, we can gain the magnetoconductivities $\sigma_{xx} = \rho_{xx}/(\rho_{xx}^2 + \rho_{xy}^2)$ and $\sigma_{xy} = \rho_{xy}/(\rho_{xx}^2 + \rho_{xy}^2)$. Then $\sigma_{xx}(B)$ and $\sigma_{xy}(B)$ can be fitted by the two-carrier model, respectively

$$\sigma_{xx} = \left[\frac{n_h\mu_h}{1+(\mu_h B)^2} + \frac{n_e\mu_e}{1+(\mu_e B)^2}\right] e, \quad (2)$$

$$\sigma_{xy} = \left[\frac{n_{\rm h}\mu_{\rm h}^2}{1+(\mu_{\rm h}B)^2} - \frac{n_{\rm e}\mu_{\rm e}^2}{1+(\mu_{\rm e}B)^2}\right] eB, \tag{3}$$

where e is the elementary charge, $n_{\rm e}$ and $n_{\rm h}$ are the carrier densities of the electrons and holes, $\mu_{\rm e}$ and $\mu_{\rm h}$ are the mobilities of the electrons and holes, respectively. The fitting results are shown by the red curves in Figs. 2(c) and 2(d), which correspond to the fitting parameters $n_{\rm e} = 4.10\times10^{19}$ cm^{-3}, $n_{\rm h} = 4.29\times10^{19}$ cm^{-3}, $\mu_{\rm e} = 680$ cm$^2\cdot$V$^{-1}\cdot$s^{-1}, $\mu_{\rm h} = 1109$ cm$^2\cdot$V$^{-1}\cdot$s^{-1} at 1.5 K. The results are basically consistent with the compensated electron–hole model in $TaCo_2Te_2$. The two-carrier model requires a simultaneous fitting of both σ_{xx} and σ_{xy} using a single set of parameters. That is to say, the longitudinal and Hall data shown in Figs. 2(c) and 2(d) are fitted simultaneously using Eqs. (2) and (3). The same applies to Figs. 3(d) and 3(e). While the simultaneous fitting ensures a reliable extraction of the material parameters, it inherently imposes a trade-off between optimizing the fit for σ_{xx} and σ_{xy}. As a result, deviations of the fitting are common and hard to eliminate.

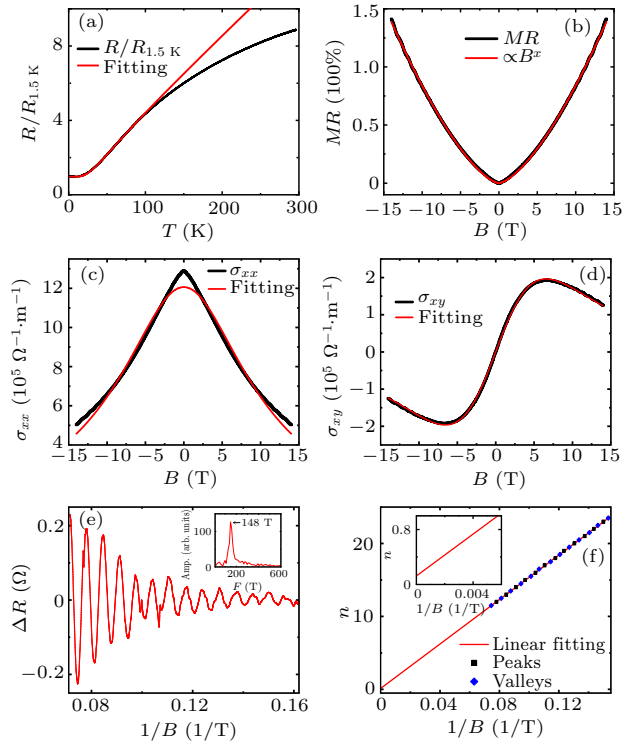


Fig. 2. The transport measurement of the $TaCo_2Te_2$ Hall bar device #1. (a) Normalized resistance as a function of temperature. The red curve represents the fitting using Eq. (1). (b) The longitudinal magnetoresistance under a perpendicular magnetic field at 1.5 K. The red curve shows a power-law fitting $\propto B^x$ which yields $x = 1.5$. (c) and (d) The longitudinal and Hall magnetoconductivity at 1.5 K. The red curves correspond to the simultaneous fitting using Eqs. (2) and (3). (e) Extracted SdH oscillations from the background-subtracted R_{xx} as a function of $1/B$. The inset displays the fast Fourier transform (FFT) spectrum of the oscillations. (f) Landau level index n *versus* $1/B$, extracted from the peak (n) and valley ($n-1/2$) positions of the SdH oscillations in panel (e). The red line is a linear fit to the peak (valley) positions. The inset zooms into the low-$1/B$ region.

Pronounced SdH oscillations were observed in the high-field region ($B > 8$ T), as shown in Fig. 2(e), demonstrating the retained high quality of the $TaCo_2Te_2$ flake down to 15 nm. Note that we subtracted a smooth background to isolate the SdH oscillations from the R_{xx}–B data, and plotted ΔR *versus* $1/B$ in Fig. 2(e). Fast Fourier transform (FFT) analysis of the oscillations revealed a dominant frequency near 148 T (shown in the inset of Fig. 2(e)), consistent with the previously reported β branch in the literature.[10,14]

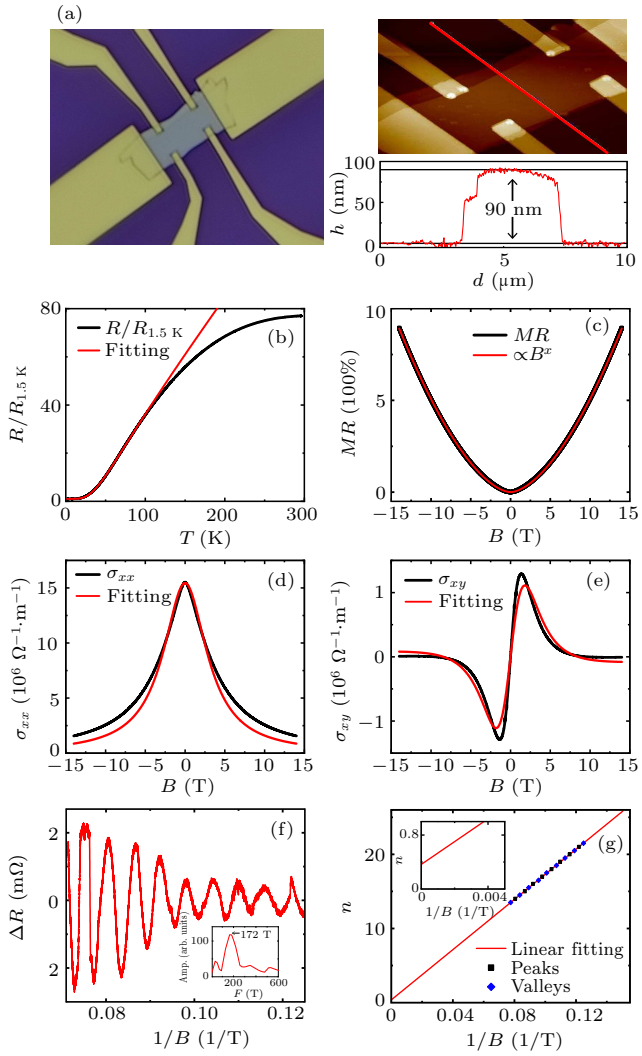


Fig. 3. The transport measurement of the $TaCo_2Te_2$ Hall bar device #2. (a) Optical image of device #2 and the AFM measurement of the thickness. (b) Normalized resistance as a function of temperature. The red curve represents the fitting using Eq. (1). (c) The longitudinal magnetoresistance under a perpendicular magnetic field at 1.5 K. The red curve shows a power-law fitting $\propto B^x$ which yields $x = 1.68$. (d) and (e) The longitudinal and Hall magnetoconductivities at 1.5 K. The red curves correspond to the simultaneous fitting using Eqs. (2) and (3). (f) Extracted SdH oscillations from the background-subtracted R_{xy} as a function of $1/B$. The inset displays the FFT spectrum of the oscillations. (g) Landau level index n *versus* $1/B$, extracted from the peak (n) and valley ($n-1/2$) positions of the SdH oscillations in panel (f). The red line is a linear fit to the peak (valley) positions. The inset zooms into the low-$1/B$ region.

These oscillations are quantitatively modeled by the Lifshitz–Kosevich theory,[15] which predicts a periodic modulation proportional to $\cos[2\pi(F/B)+\phi]$. The frequency F and phase parameter ϕ are critical for probing the topological and geometric properties of the material's Fermi surface.

Notably, theoretical studies[16,17] suggest that linearly dispersive energy bands (*e.g.*, in Dirac or Weyl systems) introduce an additional Berry phase of π. Although there remains controversy over whether the peaks or valleys of SdH oscillations correspond to the integer index of Landau levels, theoretical calculations suggest that ρ_{xx} at the band edge should correspond to a peak.[18] From Fig. 2(e), the $1/B$ values of SdH extrema (peaks and valleys) of the SdH oscillations were extracted and linearly fitted as a function of the Landau level index n, as presented in Fig. 2(f). This method has been employed in the literature to examine the Berry phase.[18,19] According to the Lifshitz–Onsager quantization rule,[20] from the linear fit of the Landau fan diagram, the slope (F) and intercept ($\gamma+\delta$) were determined to be $F = 152.4 \pm 0.39$ T and $\gamma+\delta = 0.124 \pm 0.045$, respectively. The Berry phase $2\pi\beta$ can be extracted from the intercept in Landau fan diagram through the formula $\gamma+\delta = -1/2+\phi_B/2\pi$, yielding a non-zero Berry phase of -0.752π for a quasi-2D cylindrical Fermi surface ($\delta = 0$). Therefore, a non-zero Berry phase is obtained.

To investigate the thickness-dependent transport properties of $TaCo_2Te_2$, we additionally fabricated and measured a 90-nm-thick Hall bar device (#2) for comparisons, as illustrated in Fig. 3(a). The R–T curve of this device is shown in Fig. 3(b). The *RRR* is 77, which is significantly larger than that of device #1. The R–T curve is also well fitted by the Bloch–Grüneisen formula, revealing a low-temperature behavior consistent with that of device #1. The fitting yields $\rho_0 = 6.56 \pm 0.01$ μΩ·cm, $A = 2385.4 \pm 1.4$ μΩ·cm, and $\theta_D = 208.5 \pm 0.1$ K. Subsequently, we measured the ρ_{xx} and ρ_{xy} of the device at 1.5 K under a perpendicular magnetic field ($-14\ \text{T} \le B \le 14\ \text{T}$) and gained the *MR*, as shown in Fig. 3(c). The *MR* is 425% at 9 T and 1.5 K, far larger than that in device #1. The *MR* scaling behavior has a power-law dependence, $MR \propto B^{1.68}$, consistent with the as-grown sample ($MR \propto B^{1.73}$) in Ref. [11]. The longitudinal and Hall conductivity were analyzed using a two-carrier model, as shown in Figs. 3(d) and 3(e), yielding fitting parameters $n_e = 1.69 \times 10^{20}$ cm^{-3}, $n_h = 1.57 \times 10^{20}$ cm^{-3}, $\mu_e = 2572$ cm$^2 \cdot$V$^{-1} \cdot$s^{-1}, $\mu_h = 3380$ cm$^2 \cdot$V$^{-1} \cdot$s^{-1}.

Table 1. A systematic comparison of the transport parameters measured in device #1 and device #2 along with previously reported values in the literature.

Our devices or references	Thick (nm)	*RRR*	θ_D (K)	*MR* (9 T) (≤ 3 K)	n_e (10^{20} cm^{-3})	n_h (10^{20} cm^{-3})	μ_e (cm$^2\cdot$V$^{-1}\cdot$s^{-1})	μ_h (cm$^2\cdot$V$^{-1}\cdot$s^{-1})
device # 1	15	9	155	72%	0.41	0.429	680	1109
device # 2	90	77	208.5	425%	1.69	1.57	2572	3380
[12]	155	48	188	833%	3.45	3.07	3640	4620
[14]	bulk	25	194	705%	1.36	1.12	2790	4120
[10]	bulk	17	none	263%	1.44	1.20	1553	2293
[11] (as-grown)	bulk	73	none	3720%	7.71	7.71	3540	3540
[11] (annealed)	bulk	48	none	571%	0.097	0.62	1750	2210

In order to show a clear comparison, we have compiled the transport parameters measured from device #1 and device #2 alongside previously reported values in Table 1. Notably, the carrier concentrations of device #2 align well with those of the bulk samples in Refs. [10,14], but are slightly lower than those of the 155-nm-thick flake reported in Ref. [12] and those of the as-grown sample in Ref. [11]. In contrast, the carrier concentrations of device #1 are comparable to those of the annealed sample reported in Ref. [11], but approximately one order of magnitude lower than those of device #2 and other reported values. Regarding carrier mobilities, device #2 exhibits values consistent with Refs. [10–12, 14], while device #1 shows significantly lower mobilities than all reported results. Furthermore, by comparing other parameters, it is evident that the *MR*, Debye temperature θ_D, and *RRR* in device #1 are significantly lower than those in device #2 and previously reported values in the literature. This discrepancy may arise from enhanced disorder and a higher density of structural domains in the thinner sample. The significant reduction in *MR* and the change in the power-law dependence $MR \propto B^x$ ($x = 1.5$ in device #1 and $x = 1.68$ in device #2) can also be attributed to the increased defects and disorder in the 15-nm sample, which modifies the magnetotransport properties. In addition, dimensionality effects and the misalignment of the voltage leads may also influence the power-law dependence of *MR*.[21] This behavior aligns with prior observations reported for the as-grown and post-annealed $TaCo_2Te_2$ single crystals.[11] The thinner sample, prone to introducing grain boundaries, dislocations, or residual stress, suffers from phonon scattering due to these defects, leading to reduced effective lattice stiffness.[22] All in all, through analyzing and comparing the transport parameters in the 15-nm and the 90-nm samples as well as the transport parameters previously reported in the literatures, we found that as the sample thickness decreases, the phonon scattering caused by defects is likely enhanced. Nevertheless, SdH oscillations and non-zero Berry phase are preserved in thin flakes down to 15 nm.

We now come back to the SdH oscillations in device #2, extracted from the R_{xy}–B curve, and shown in Fig. 3(f). The FFT analysis of the oscillations revealed a dominant frequency near 172 T (shown in the inset of Fig. 3(f)). It is worth emphasizing that we prioritized R_{xy}–B over R_{xx}–B for oscillation

analysis due to its superior signal-to-noise ratio. From the FFT results, we observe the increase in the SdH oscillation period for device #1 compared to device #2, which might be attributed to the significant influence of spatial confinement on the band structure, reducing the overlap between the conduction and valence bands.[23] When the thickness decreases, finite-size effects diminish the cross-sectional area of the Fermi surface perpendicular to the magnetic field direction, which leads to an increase in $\Delta(1/B)$. From the linear fit of the Landau fan diagram shown in Fig. 3(g), the slope (F) and intercept ($\gamma+\delta$) were determined to be $F = 169.4\ \mathrm{T} \pm 0.58$ and $\gamma = 0.364 \pm 0.059$ ($\delta = 0$), respectively. The Berry phase is calculated to be a non-zero value of -0.272π. We note that the Berry phase in device #2 exhibits a noticeable deviation from the value of -0.752π measured in device #1. This discrepancy might arise from modifications to the band structure induced by reduced dimensionality. Such dimensionality-dependent Berry phase have been reported in Cd_3As_2 thin films, where decreasing thickness drives a dimensional crossover.[19]

4. Conclusions

In summary, we have systematically investigated and compared the low-temperature transport properties of exfoliated $TaCo_2Te_2$ flakes with two distinct thicknesses: 15 nm and 90 nm. The 15-nm sample shows lower *RRR*, Debye temperature, *MR*, carrier concentrations, and mobilities than the 90-nm one, which can be attributed to enhanced defect-induced phonon scattering. Notably, despite this disorder, the 15-nm sample still exhibits pronounced SdH oscillations ($B > 8$ T). Analysis of the Landau level index (n) *versus* $1/B$ yields a non-zero Berry phase in both samples, indicating the possible existence of a topologically non-trivial phase in $TaCo_2Te_2$ thin flakes. These findings establish $TaCo_2Te_2$ as a compelling platform for studying robust topological phases in layered materials, where dimensionality and intrinsic topology synergistically preserve quantum coherence against structural imperfections.

Acknowledgements

Project supported by the National Key Research and Development Program of China (Grant Nos. 2022YFA1403400 and 2020YFA0309200), the National Natural Science Foundation of China (Grant Nos. 12074417, 92065203, 92365207, and 92477115), the Strategic Priority Research Program of Chinese Academy of Sciences (Grant No. XDB33000000), the Synergetic Extreme Condition User Facility sponsored by the National Development and Reform Commission, and the Innovation Program for Quantum Science and Technology (Grant No. 2021ZD0302600).

References

[1] Wang A, Li Y, Yang G, Yan D, Huang Y, Guo Z, Gao J, Huang J, Zeng Q, Qian D, Wang H, Guo X, Meng F, Zhang Q, Gu L, Zhou X, Liu G, Qu F, Qian T, Shi Y, Wang Z, Lu L and Shen J 2023 *Nat. Commun.* **14** 7647
[2] Jiao W H, Qiu H Q, Yang W, Bao J K, Xiao S, Liu Y, Li Y, Cao G H, Xu X, Ren Z and Zhang P 2023 *Phys. Rev. B* **108** 245145
[3] Koepernik K, Kasinathan D, Efremov D V, Khim S, Borisenko S, Büchner B and Van Den Brink J 2016 *Phys. Rev. B* **93** 201101
[4] Schönemann R, Chiu Y C, Zheng W, Quito V L, Sur S, McCandless G T, Chan J Y and Balicas L 2019 *Phys. Rev. B* **99** 195128
[5] Hao Z, Chen W, Wang Y, Li J, Ma X M, Hao Y J, Lu R, Shen Z, Jiang Z, Liu W, Jiang Q, Yang Y, Lei X, Wang L, Fu Y, Zhou L, Huang L, Liu Z, Ye M, Shen D, Mei J, He H, Liu C, Deng K, Liu C, Liu Q and Chen C 2021 *Phys. Rev. B* **104** 115158
[6] Xiao S, Jiao W H, Lin Y, Jiang Q, Yang X, He Y, Jiang Z, Yang Y, Liu Z, Ye M, Shen D and He S 2022 *Phys. Rev. B* **105** 195145
[7] Lu Q, Ran Z, Li Y, Xu C, Hu J, Yin X, Wang G, Zhang W, Luo W, Xu X and Qian D 2022 *Quantum Front.* **1** 9
[8] Tremelt W 1991 *Journal of the Chemical Society, Chemical Communications* **19** 1405
[9] Tremel W 1992 *Angew. Chem. Int. Ed. Engl.* **31** 217
[10] Singha R, Yuan F, Cheng G, Salters T H, Oey Y M, Villalpando G V, Jovanovic M, Yao N and Schoop L M 2022 *Adv. Funct. Mater.* **32** 2108920
[11] Wang L, Tian J, Kang C, Gu H, Pang R, Shen M, She L, Song Y, Liu X and Zhang W 2022 *Inorg. Chem.* **61** 18899
[12] Pate S, Chen B, Shen B, Li K, Zhou X, Chung D Y, Divan R, Kanatzidis M G, Welp U, Kwok W K and Xiao Z L 2024 *Phys. Rev. B* **109** 035129
[13] Rong H, Huang Z, Zhang X, Kumar S, Zhang F, Zhang C, Wang Y, Hao Z, Cai Y, Wang L, Liu C, Ma X, Guo S, Shen B, Liu Y, Cui S, Shimada K, Wu Q, Lin J, Yao Y, Wang Z, Xu H and Chen C 2023 *npj Quantum Mater.* **8** 29
[14] Jiao W H, Liu Y, Tao P, Lu J, Liang X, Yang W, Zhang Z, Xu S, Luo Y, Zhu Z W, Qian D, Xu X, Ren Z, Cao G H and Xiao S 2025 *Phys. Rev. B* **111** 045109
[15] Shoenberg D 1984 *Magnetic Oscillations in Metals* (Cambridge: Cambridge University Press)
[16] Xiao D, Chang M C and Niu Q 2010 *Rev. Mod. Phys.* **82** 1959
[17] Mikitik G P and Sharlai Y V 1999 *Phys. Rev. Lett.* **82** 2147
[18] Wang C M, Lu H Z and Shen S Q 2016 *Phys. Rev. Lett.* **117** 077201
[19] Cheng P, Zhang C, Liu Y, Yuan X, Song F, Sun Q, Zhou P, Zhang D W and Xiu F 2016 *New J. Phys.* **18** 083003
[20] Murakawa H, Bahramy M S, Tokunaga M, Kohama Y, Bell C, Kaneko Y, Nagaosa N, Hwang H Y and Tokura Y 2013 *Science* **342** 1490
[21] Wang Q, Guo P J, Sun S, Li C, Liu K, Lu Z Y and Lei H 2018 *Phys. Rev. B* **97** 205105
[22] Ma W, Zhang X and Takahashi K 2010 *J. Phys. D: Appl. Phys.* **43** 465301
[23] Xiang F X, Srinivasan A, Du Z Z, Klochan O, Dou S X, Hamilton A R and Wang X L 2018 *Phys. Rev. B* **98** 035115